

LISA test-mass charging. Particle flux modeling, Monte Carlo simulations and induced effects on the sensitivity of the observatory

F. Dimiccoli^{1,2}, R. Dolesi^{1,2}, M. Fabi^{3,4}, V. Ferroni^{1,2}, C. Grimani^{3,4}, M. Muratore⁵, P. Sarra⁶, M. Villani^{3,4} and W.J. Weber^{1,2}

¹ Trento Institute for Fundamental Physics and Applications (TIFPA-INFN), Trento, Italy

² Department of Physics, University of Trento, Trento, Italy

e-mail: francesco.dimiccoli@unitn.it *

³ University of Urbino Carlo Bo, Department of Pure and Applied Sciences (DiSPeA), Via Santa Chiara, 27, Urbino (PU), 61029, Italy

⁴ National Institute for Nuclear Physics (INFN), Section in Florence, Via B. Rossi 1, Florence, 50019, Italy

⁵ Max Planck Institute for Gravitational Physics (Albert Einstein Institute), D-14476 Potsdam, Germany

⁶ OHB Italia SpA Milano, Italy

ABSTRACT

Context. The LISA space observatory will explore the sub-Hz spectrum of gravitational wave emission from the Universe. The space environment, where will be immersed in, is responsible for charge accumulation on its free falling test masses (TMs) due to the galactic cosmic rays (GCRs) and solar energetic particles (SEP) impinging on the spacecraft. Primary and secondary particles produced in the spacecraft material eventually reach the TMs by depositing a net positive charge fluctuating in time. This work is relevant for any present and future space missions that, like LISA, host free-falling TMs as inertial reference.

Aims. The coupling of the TM charge with native stray electrostatic field produces noise forces on the TMs, which can limit the performance of the LISA mission. A precise knowledge of the charging process allows us to predict the intensity of these charge-induced disturbances and to design specific counter-measures.

Methods. We present a comprehensive toolkit that allows us to calculate the TM charging time-series in a geometry representative of LISA mission, and the associated induced forces under different conditions of the space environment by considering the effects of short, long GCR flux modulations and SEPs.

Results. We study, for each of the previously mentioned conditions, the impact of spurious forces associated with the TM charging process on the mission sensitivity for gravitational wave detection.

Key words. Instrumentation: interferometers – (ISM:) cosmic rays – Sun: particle emission – Elementary particles

1. Introduction: an end-to-end toolkit for the simulation of the LISA test-mass charging

Experimental gravitational wave physics had a turning point in 2015 when the LIGO interferometers detected the gravitational radiation emission from the merging of a stellar black hole binary system (Abbott et al. 2016). That was the first direct confirmation of the existence of gravitational waves predicted by Einstein's theory of General Relativity (Einstein 1916).

The ESA LISA Pathfinder (LPF) mission (Antonucci et al. 2011a,b) was launched on December 4th of the same year (Armano et al. 2016, 2018b). This mission demonstrated that a reference mass (same as test-masses, TMs, in the following) can be put into geodesic motion with a residual stray acceleration of the level required by a space interferometer for gravitational wave observation built in space. The Laser Interferometer Space Antenna (LISA) has been approved by ESA in its phase A in 2017 (Amaro-Seoane et al. 2017), with the aim to open a window on the mHz band (Colpi et al. 2024), and finally adopted in January 2024, with expected launch in 2035. LISA will use free-falling test masses as end mirrors of a large space interfer-

ometer with 2.5 million km arms. The LISA TMs will be hosted on a constellation of three spacecraft (S/C) in triangular formation in orbit around the Sun, trailing Earth at about 50 million km. The LISA sensitivity is expected to unveil the gravitational wave spectrum populated by a large sample of galactic binaries, massive black holes, extreme-mass ratio inspirals and more exotic sources (Colpi et al. 2024). LISA-based observations will be complementary to those gathered by Earth interferometers, being capable of detecting gravitational waves when the binary sources arrive at merging in their measurement frequency band above a few Hz, sometimes after having emitted in the inspiral phase in the LISA band (multiband astronomy, Sesana (2016)). Moreover, LISA will be synergic with other missions observing in the electromagnetic band (Grimani et al. 2024) and Earth neutrino experiments for a multimessenger approach to the physics of compact objects (Suwa & Murase 2009).

The LISA TM has to be in free-fall to within a stray acceleration noise below $3 \text{ fm s}^{-2} \text{ Hz}^{-1/2}$ at 1 mHz. The space environment eliminates stray forces from Newtonian gravitational noise, seismic noise, and suspension thermal noise, which are the key limiting factors on ground. However, it affects differently the free-fall status of the TMs. The LISA's TMs are 46 mm gold-

* corresponding author

platinum alloy cubes coated with a 800 nm thick gold layer. The TMs are surrounded, with no mechanical contact and few mm gap, by a gold-plated electrode-housing (EH) used for both position sensing and actuation (Antonucci et al. 2012). High-energy particles of galactic and solar origin charge the LISA TMs making them sensitive to Coulomb forces due to stray electric fields found between the masses and the surrounding EH (see for details Antonucci et al. 2012). These Coulomb forces a) contribute to the acceleration noise of the TMs due to the intrinsic time fluctuations of the deposited charge and of the stray electric fields and b) generate spurious signals in the LISA sensitivity band due to solar energetic particle (SEP) events and Forbush decreases (FDs) (Forbush 1937, 1954, 1958; Armano et al. 2018a, 2019; Grimani et al. 2020a), sudden depressions of the galactic cosmic-ray (GCR) flux due to the passage of interplanetary counterparts of coronal mass ejections (ICMEs).

The charging process is associated with energetic particles able to penetrate about 16 g cm^{-2} of shielding material surrounding the TMs (Vidano et al. 2022) expected to be provided by the LISA payload and spacecraft. This corresponds to a minimum energy threshold of approximately 100 MeV, 20 MeV and 100 keV respectively for hadrons, electrons and photons of galactic and solar origin penetrating or interacting in the spacecraft (Grimani et al. 2024). The characterization of the charging process is primarily linked to the evaluation of two fundamental rate parameters (see proper definition in Eqn. 4 and 5, Section 4): λ_{NET} , indicating the rate at which the TM accumulates charge, and λ_{EFF} , which is the effective single charge Poissonian event rate associated with TM charge noise (Araújo et al. 2005).

Monte Carlo simulations of the LPF TM charging were carried out with FLUKA (Battistoni et al. 2014; Böhlen et al. 2014; Vlachoudis 2009) and GEANT4 (Agostinelli et al. 2003; Allison et al. 2016, 2006) before the mission was launched at the end of 2015. These simulations returned very similar results for both TM charging rate and noise at solar minimum conditions (Araújo et al. 2005; Grimani et al. 2015; Wass et al. 2005), despite different nominal energy thresholds for electron propagation were considered in GEANT4 (250 eV) and FLUKA (1 keV). This evidence was initially explained only in terms of the average ionization potential in gold that limited the hadron ionization to 790 eV in GEANT4 (Villani et al. 2020; Taioli et al. 2023). Conversely, in this work we show that the main problem comes from the generation and propagation of very low energy electrons.

The mission pre-launch work in Grimani et al. (2015) was carried out on the basis of predictions of the solar modulation between the end of 2015 and beginning 2016. The results of Monte Carlo simulations carried out with these updated predictions were compared to the LPF TM charging measurements carried out in space in April 20-23, 2016 (Armano et al. 2017) (see Table 1). The measured net charging appeared to lie in the middle of the prediction range, while the effective charging was three to four times higher than expected. Moreover, it was observed that the net charging depended on the potential of the TM (V_{TM}), saturating to 0 for $V_{TM} \approx 1 \text{ V}$ (Armano et al. 2023). This observational scenario was ascribable to particles with the same charge sign entering and escaping the TMs in approximately equal number, thus contributing to the charging noise but not to the net charging. Low-energy electrons (LEE, with $E < 1 \text{ keV}$) produced at the gold surfaces of the TMs and EH were the most plausible candidates to explain the observations as originally suggested in Araújo et al. (2005). In fact Monte Carlo simulations at that time were not able to account for these LEE, because of the limitation on the production and propagation of secondaries below 250 eV for GEANT4 (1 keV for FLUKA).

After the mission, simulations were refined by incorporating the actual solar modulation of the GCR flux observed during the mission elapsed time (Grimani et al. 2022; Wass et al. 2023) and extending FLUKA's electromagnetic physics below 1 keV. To achieve this, the Low Energy Ionization (LEI) Monte Carlo program was developed at the University of Urbino Carlo Bo (Villani et al. 2020; Grimani et al. 2022; Villani et al. 2024a). Studies (Grimani et al. 2020b; Villani et al. 2021) demonstrated that ionization is the primary contributor to TM charging, with kinetic emission (low-energy electron emission from surfaces bombarded by keV-MeV particles) and quantum electron diffraction below 100 eV also playing significant roles. Photon-related processes, such as transition radiation, bremsstrahlung, and Čerenkov radiation, were found to be not relevant (Grimani et al. 2020b). In LEI, low-energy ionization was implemented using the Cucinotta formula (Cucinotta et al. 1996), while Sakata cross-sections were applied for electrons and positrons (Sakata et al. 2016). Kinetic emission was initially implemented using Schou's formalism (Schou 1980; Grimani et al. 2020b) but was later found to be overestimated by 30% (Grimani et al. 2022) and thus refined using an *ab initio* approach (Taioli et al. 2023). The quantum electron diffraction model, initially assuming normal incidence (Grimani et al. 2022), was updated to account for electron direction and Bragg's planes at energies below 100 eV (Villani et al. 2024a). The TM charging obtained with FLUKA/LEI simulations reproduced nicely the observations carried out with LPF (Grimani et al. 2022; Villani et al. 2024a).

In 2021 we started under the ESA contract 4000133571/20/NL/CRS (TEST MASS CHARGING TOOLKIT AND LPF LESSONS LEARNED) the development of a toolkit (Test Mass Charging Toolkit - TMCTK), GEANT4 based, for the study of the TM charging for LPF/LISA-like GRS featuring: the low EM physics learned with FLUKA/LEI (see Section 2), a general modelization of the particle fluxes, described in Section 3, and the impact analysis of the charging process on the performance of the mission (see Section 4, 5 and 6). TMCTK was finally delivered to ESA in 2023 adopting version 11 of GEANT4 released in December 2021 along with an improved version of the GEANT4-DNA module (Tran et al. 2024; Incerti et al. 2018; Bernal et al. 2015; Incerti et al. 2010b,a), made to address the simulation of extremely low-energy electromagnetic processes (down to 10 eV) typically used for radiobiology studies (Sakata et al. 2018).

The first aim of this paper is to present the main elements of TMCTK and its first results for LISA mission, that allow to accurately predict the impact on the LISA mission of a wide array of environmental charging scenarios. However, despite the improvements, the TMCTK prediction for the charging noise λ_{EFF} appear underestimated with respect to FLUKA/LEI and LPF observations. Further investigations on this issue revealed in fact major discrepancies between TMCTK and FLUKA/LEI regarding some particular aspects of LEE propagation, like backscattering and the transmission yields on gold slabs. The details of these discoveries are discussed in Section 5 of the paper and will be the subject of future investigation along with the GEANT4 scientific community.

2. LISA test-mass charging Monte Carlo simulation

The estimation of the effects of the space environment on the LISA TM free fall motion is founded on the Monte Carlo simulation of the particle to matter interaction. As the LISA spacecraft design is not defined at present, we have considered a spherical

Table 1. Net and effective TM charging and TM equilibrium potential measured with LPF (Armano et al. 2017, 2023).

	Test mass 1	Test mass 2
λ_{NET} (s^{-1})	$+22.9 \pm 1.7$	$+24.5 \pm 2.1$
λ_{EFF} (s^{-1})	1060 ± 90	1360 ± 130
V_{TM}^{EQ} (V)	0.9 ± 0.3	0.96 ± 0.4

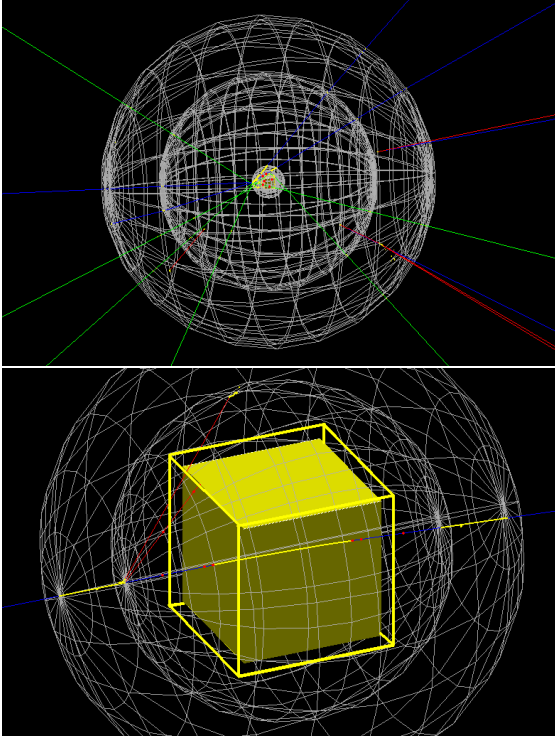


Fig. 1. Top panel: LISA spacecraft simplified matter distribution around the TMs. Bottom panel: Magnified view of the central part of the geometry modeling the GRS and the TM in GEANT4. The 150 nm wide cubic box modeling the last interface of the EH, as well as the spherical shielding shells, are visualized in wireframe mode for visualization purposes.

symmetry for the material distribution around the TM consisting of four aluminum concentric spherical shells surrounding a gold cubic TM. This material amount is quantified in a total of 16 g/cm^2 , mainly concentrated in the vicinity of the TMs. This is an extremely simplified modelization of the matter distribution. The amount of matter was set on the basis of a preliminary design of LISA spacecraft (Vidano et al. 2022). The adoption of a simplified geometry is a common practice¹ in the design process of space missions to carry out an estimation of the effects of the space environment on sensitive parts of the satellite (Vocca et al. 2004). Moreover, given the importance of emission of secondary particles generated by particle interaction in the immediate vicinity of the TM, the innermost interface of the GRS EH is modeled as a cubic gold box 150 nm thick and 5.2 cm on the side representing part of the outer film of gold, separated from the TM itself by a 3 mm vacuum gap. This arrangement, the same adopted in Taioli et al. (2023) allows us to save computation time without losing the significance of the simulation. The thickness of the layer was chosen to be conservatively greater than the mean free path of electrons with energies below 100 eV.

¹ See for instance <https://www.spennis.oma.be/>

Extensive studies of the output of the simulation demonstrated the negligible dependence of the results on this parameter.

The particle propagation in GEANT4 occurs in discrete steps properly selected from the active processes. In particular, the active processes characterized by high cross sections for an assigned material and particle energy, have a higher probability to be selected by the simulation engine. The length of the propagation step depends on the selected physical process, but can also be limited by the user to a custom value. The particle ionization energy loss is implemented according to the continuous slowing down approximation (CSDA). After each step, the energy of the simulated particle is lowered accordingly. In general, such approach allows for a reliable description of the production of secondaries and of the particle energy loss over the steplength by maintaining a relatively high efficiency from the point of view of the computation power.

GEANT4 allows for a modular handling of the different categories of physical processes (electromagnetic, hadronic, decay), that can be independently activated in the simulations. These modules are included into a "modular physics list" where each process for a given energy and material uses appropriate theoretical models that can be chosen by the users. The activation of a large number of modules enhances the precision of the simulations and the number of possible considered interactions, at the cost of a major increase of the processing time. The physics list implemented for this study is the standard QGSP-BIC (Geant4 Collaboration (2024)), which includes all the principal electromagnetic and hadronic processes, as well as radioactive decay and neutron transport. Of particular interest for us, is the implementation of the module that activates the electromagnetic interactions. In our simulation we made use of the "G4StandardEM-option4" (Opt4) module (Ivanchenko et al. 2014), which is particularly suited for studies where electrons and positrons play a relevant role, allowing us to track these particles down to energies of 100 eV. Opt4 is used in all spacecraft regions except for the outer 150 nm of gold of both TM and EH where the QGSP-BIC physics list was integrated with the GEANT4-DNA module, to account for production and propagation of LEE. The processes implemented in the DNA module will be briefly described in the following subsection.

2.1. Simulation of low-energy electrons

GEANT4-DNA replaces the comprehensive multiple scattering processes of Opt4 with more detailed models for LEE interactions, including: elastic scattering, electronic excitation, ionization, vibrational excitation, and molecular attachment.

For electrons in gold, GEANT4-DNA includes specific cross-section models covering energies from 10 eV to 1 GeV. Although GEANT4-DNA can also simulate processes involving nuclei, such as protons and alpha particles, no cross-section models for these particle interactions in gold are currently available. Therefore, custom processes described in Section 2.2 were implemented, analogously to Wass et al. (2023) to model LEE kinetic emission following the impact of these particles, which, anyways, contribute minimally to the overall LEE production.

By default GEANT4 allows for the propagation of electrons until their energy is reduced by CSDA below a threshold E_{min} , which for GEANT4-DNA module is set by default at 10 eV. Below this threshold, the propagation of the particle is stopped. The discrete interactions have a different low energy threshold E_{th} which encodes the energy validity range of their cross section models. In GEANT4-DNA E_{th} is nominally set at 10 eV as E_{min} . However, the minimum energy required for a LEE to escape

the gold surfaces of the TM and EH is equal to the gold work function, found to be typically in the range 3.9-5.2 eV (Wass et al. 2023). As such, in our toolkit, the E_{min} threshold was lowered to 4 eV, without altering (E_{th}). This adjustment allows secondary electrons with energies between (E_{min}) and (E_{th}) reaching the gold-vacuum boundary to escape the surface.

As demonstrated in Taioli et al. (2023), this approach effectively reproduces the theoretical and measured electron backscattering yield of gold. Varying the E_{min} threshold between 3.8 and 4.2 eV showed no significant impact on the λ_{NET} and λ_{EFF} .

2.2. Low-energy electrons from hadrons

Kinetic emission of low-energy electrons (LEEs) can also occur when nuclei, such as protons and alpha particles in the keV-MeV energy range, interact with the gold surfaces of test masses (TMs) and electrode housings (EH). Since cross section models for these processes in gold are not included in GEANT4-DNA, two custom processes were implemented in the GEANT4 physics list. These processes simulate the emission of secondary LEEs using a yield-based approach, triggered when protons or alpha particles traverse the gold surfaces. The number of generated electrons $Y(E, \theta)$, as a function of proton energy E and incidence angle θ with respect to the normal to the surface, is sampled from the average proton and alpha kinetic emission yield function, defined by the following formula (Furman & Pivi 2002; Wass et al. 2023):

$$Y(E, \theta) = Y_{max}(\theta) \frac{sE/E_{max}(\theta)}{s - 1 + (E/E_{max}(\theta))^2}$$

where

$$E_{max}(\theta) = E_0[1 - 0.7(1 - \cos(\theta))]$$

and

$$Y_{max} = Y_0[1 + 0.66 \cos^{0.8}(\theta)].$$

In the above formulas Y_0 is the value of yield for particles normally incident on the surface, E_0 represents the peak energy of the distribution and s its spectral width. In the case of protons, values of $Y_0=2.18$, $E_0=180$ keV and $s=1.54$ have been

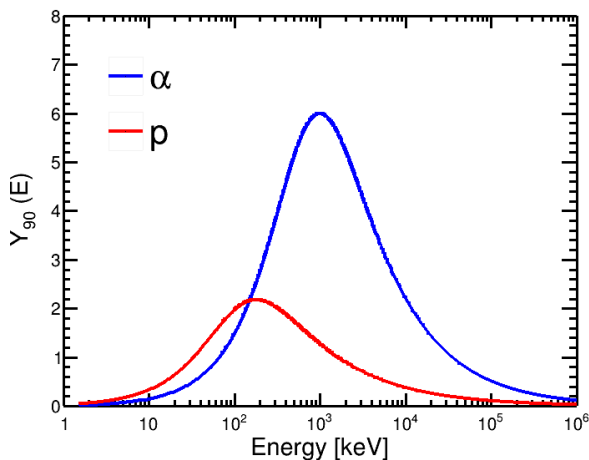


Fig. 2. Low-energy electron yield of the kinetic emission processes for p (red) and α particles (blue) crossing perpendicularly gold surfaces (Y_{90}) as a function of p and α energy.

used (Furman & Pivi 2002). For the kinetic emission given by alpha particles, very subdominant with respect to the electron production from protons, the angular dependence was considered constant, and values of $Y_0=6$, $E_0=200$ keV and $s=1.64$ were used. The energy distribution of the LEE produced by these processes is sampled from a narrow ($\sigma = 2$ eV) distribution centered around 8.4 eV, and their emission direction is assumed isotropic with respect to the surface normal direction.

Figure 2 shows the yield functions and the energy spectrum of the LEEs generated by kinetic emission from protons and helium nuclei (α particles) as implemented in the toolkit.

2.3. Electron Quantum diffraction

Due to the low energy of electrons involved in the TM charging process, wave-like quantum mechanical behaviour of these particles, such as diffraction, cannot be disregarded.

Diffraction occurs when the wavelength of the electron is comparable to the spacing between the atoms in a crystal lattice (≈ 4 Å for gold). In order to calculate the probability of diffraction at a given electron energy E , one must solve the radial Schrödinger equation of an electron into the potential of the crystal lattice:

$$-\frac{\hbar^2}{2m} \frac{1}{r^2} \frac{d}{dr} \left(r^2 \frac{dR_l(r)}{dr} \right) + \frac{\hbar^2}{2m} \frac{l(l+1)}{r^2} R_l(r) + \left(-\frac{Ze^2}{r} + V_{ex}(r) \right) R_l(r) = ER_l(r) \quad (1)$$

where Z is the atomic number ($Z = 79$ for gold), m is the electron mass, l is the angular momentum quantum number and $V_{ex}(r)$ is the exchange potential due to the fact that electrons are identical particles; finally $R_l(r)$ is the radial wavefunction.

The Schrödinger equation (1) is solved in two different ranges: inside the potential of a single ion and in the region between atoms, where the potential is constant; the two solutions are matched by imposing that they assume the same value at the boundary of the two regions and that their derivatives are continuous. With this approach, it is possible to estimate the electron reflection probability. For the details of this procedure see Van Hove et al. (1986); Grimani et al. (2020b); Villani et al. (2024a).

The theoretical calculation described above provides the electron backscattering probability as a function of electron energy and incidence angle with respect to the normal of the gold surface due to quantum diffraction. The GEANT4 toolkit was integrated with this custom process active only in proximity to the two facing surfaces of TM and EH, similarly to the process described in Section 2.2. The incoming electron is reflected back at the same incidence angle according to the estimated quantum backscattering probability, without energy change.

3. Modeling the space particle environment for LISA

The LISA TM charging will depend on the overall particle flux incident on each spacecraft. Given the about 16 g cm^{-2} (Vidano et al. 2022) of spacecraft material that are expected to shield the TMs on board the three LISA spacecraft, only primary particles above a certain energy threshold will contribute to the charging. This limits are about 100 MeV/n for hadrons, 20 MeV for electrons and 100 keV for photons (Grimani et al. 2024). The LISA interferometer is expected to nominally operate for 4.5 years and up to 10 years, so to fully encompass the variability of environmental conditions during that period and to evaluate the range

of the net charging and charging noise that plausibly will be observed, we will consider different conditions of the interplanetary medium: long and short-term variations of GCR fluxes and real SEP events of different intensity.

In general, GCR fluxes and solar particles associated with gradual events (Reames 2021, 2022), lie in the energy range of interest for the TM charging, and their energy dependence must be taken into account to properly assess the TM charging. The composition of GCR consist approximately of 90% protons, 8% helium nuclei, 1% heavy nuclei and 1% electrons, where the percentages are meant in particle numbers to the total number (Simpson 1983; Papini et al. 1996). Conversely, the particles of SEP events are mainly protons (99%), with electrons and nuclei constituting the residual 1% (Reames 2021).

TMTCK simulates the different fluxes according to a parametrization discussed in the following Sub-sections.

3.1. Long term variations of Galactic Cosmic Rays

The cosmic-ray intensity long-term variations (> 1 month) show quasi-eleven and quasi-twenty two year periodicities associated with the solar activity and the global solar magnetic field (GSMF) polarity change. During the last three solar cycles the overall GCR flux below tens of GeV has been observed to vary by a factor of four in the inner heliosphere (Grimani et al. 2023b, 2021, 2023a).

LISA is supposed to be launched in 2035 near the maximum of the solar cycle 26 during a positive polarity period of the GSMF, the same of LPF. In Grimani et al. (2008) it was shown that during positive polarity periods the energy spectra, $J(r, E, t)$, of cosmic rays at a distance r from the Sun at a time t are well represented by the symmetric model in the *force field approximation* by Gleeson and Axford (G&A Gleeson & Axford 1968). By considering time-independent interstellar cosmic-ray spectra $J(\infty, E + \Phi)$ and an energy loss parameter Φ it is found that:

$$\frac{J(r, E, t)}{E^2 - E_0^2} = \frac{J(\infty, E + \Phi)}{(E + \Phi)^2 - E_0^2}, \quad (2)$$

where E and E_0 represent the particle total energy and rest mass, respectively. For $Z=1$ particles with rigidity (particle momentum per unit charge) larger than 100 MV, the role of the solar activity is taken into account by defining a *solar modulation parameter* ϕ measured in MV that, at these energies, is equal to Φ (Armano et al. 2018a).

The proton interstellar spectrum by Burger et al. (2000) has been adopted to set the solar modulation parameter estimated by Usoskin et al. (2011, 2017) and used here². Unfortunately, in the Burger et al. (2000) paper, no helium flux at the interstellar medium is provided. As a result, we have used the Shikaze et al. (2007) helium interstellar spectrum, selected on the basis of the BESS experiment data. In order to test the reliability of the model and of our approach for proton and helium flux estimates, we have compared the outcomes of the model to the monthly average space station magnetic spectrometer experiment AMS-02 data gathered in 2016 above 450 MeV/n (Aguilar et al. 2021). While the model outcome and data for proton flux show an agreement within 10%, the helium flux obtained with the model resulted higher by 25% with respect to the data. Therefore we normalized the helium flux for LPF in 2016 to the contemporaneous AMS-02 data gathered above 450 MeV/n. For LISA we

will consider the same approach since the LISA particle detectors will provide proton and helium differential fluxes up to 400 MeV/n.

The modulated particle spectra obtained with the G&A model have been parameterized according to the following equation (Papini et al. 1996):

$$F(E) = \frac{A}{(E + b)^\alpha} E^\beta \text{ Particles } (m^2 \text{ sr s GeV n}^{-1})^{-1} \quad (3)$$

where the parameter b measured in GeV/(n) is used to depress the particle flux at low energies and the dimensionless parameters α and β allow us to reproduce the trend of the spectrum at high energies. Finally, A , measured in particles/(m² sr s (GeV(n⁻¹))^{− α + β +1}), is the normalization constant. The agreement between equation 3 with the G&A model was discussed in detail in Armano et al. (2019).

Since the solar activity at the time LISA will be in orbit is not known yet, we consider a solar modulation parameter of $\phi=200$ MV at solar minimum and $\phi=1200$ MV at solar maximum as extreme cases for all particle species on the basis of former observations of the solar modulation parameter. In Figure 3 and Tables 2 our estimates for proton, nuclei energy spectra and associated parameterization as from Eqn. 3 are presented for LISA.

The galactic and interplanetary electron contribution to the LPF TM charging was discussed in detail Grimani et al. (2009). Also for LISA we consider only galactic electrons, while electrons below ≈ 20 MeV, typically of interplanetary and solar origin are disregarded. The electron flux at the interstellar medium by Moskalenko & Strong (1998) adopted here (dotted line in Figure 4) was found to better reproduce observations gathered near Earth at solar minimum, maximum and during different epochs of the GSMF (Grimani 2004, 2007). The G&A model was also used to modulate the electron interstellar spectrum at 1 AU at solar minimum ($\phi=200$ MV; dashed line in Figure 4) and at solar maximum ($\phi=1200$ MV; continuous line in Figure 4). The parameters in Eqn. 3 for electrons are shown in Table 3.

3.2. Galactic cosmic-ray short-term variations

Galactic cosmic-ray short-term variations (< 1 month) are observed at the passage of interplanetary structures. In particular, the GCR flux short-term variations are called recurrent FDs when associated with the passage of high-speed solar wind streams, and non-recurrent FDs (or simply FDs) when are generated by ICMEs (Forbush 1937, 1954, 1958). Detailed studies of the interplanetary physics of GCRs have been carried out with LPF for LISA (Armano et al. 2018a, 2019; Grimani et al. 2020a; Villani et al. 2023).

The recurrent short-term variations show an average duration of 9.1 days and a marked particle energy dependence below a few GeV, while intense FDs may present an energy dependence up to tens of GeV. The study of the energy dependence of FDs is often difficult because of the contemporaneous presence of solar particles. As case studies, we choose here to consider one recurrent FD observed with LPF and one non-recurrent FD observed in space with the PAMELA experiment (Adriani et al. 2011) and on ground with neutron monitors. The method to calculate the particle fluxparameterization during these events is described in Armano et al. (2018a, 2019); Grimani et al. (2020a). It is worthwhile to stress that we were able to use both PAMELA and neutron monitor observations for the proton flux estimate because PAMELA was in orbit near Earth (see Villani et al. 2024b). The evolution of the proton flux during the FD was estimated at the

² http://cosmicrays.oulu.fi/phi/Phi_mon.txt

Primary Particle	Solar minimum				Solar maximum			
	A	b	α	β	A	b	α	β
Protons	18000	0.65	3.66	0.87	18000	2.17	3.66	0.87
Helium	850	0.99	3.10	0.35	850	2.17	3.10	0.35
Carbon	28	1.05	3.25	0.50	28	1.15	3.75	1.00
Nitrogen	7	1.05	3.25	0.50	7	1.15	3.75	1.00
Oxygen	25.2	1.05	3.25	0.50	25.2	1.15	3.75	1.00
Iron	2.3	1.05	3.25	0.50	2.3	1.15	3.75	1.00

Table 2. Parameterizations of protons and nucleus energy spectra at 1 AU at solar minimum ($\phi=200$ MV/c) and maximum ($\phi=1200$ MV/c) for LISA. It is worthwhile to point out that A is measured in protons/(m² sr s GeV^{- $\alpha+\beta+1$}), b in GeV while α and β are pure numbers.

Solar minimum	
Energy range	Parametrization
> 20 MeV	$400(E + 0.82)^{-3.66}E^{0.5}$
Solar maximum	
Energy range	Parametrization
50 MeV - 1 GeV	$4.5(E - 0.04)^{0.84}$
> 1 GeV	$400(E + 2.5)^{-3.66}E^{0.5}$

Table 3. Parametrization of electron energy spectra above 20 MeV at solar minimum and solar maximum.

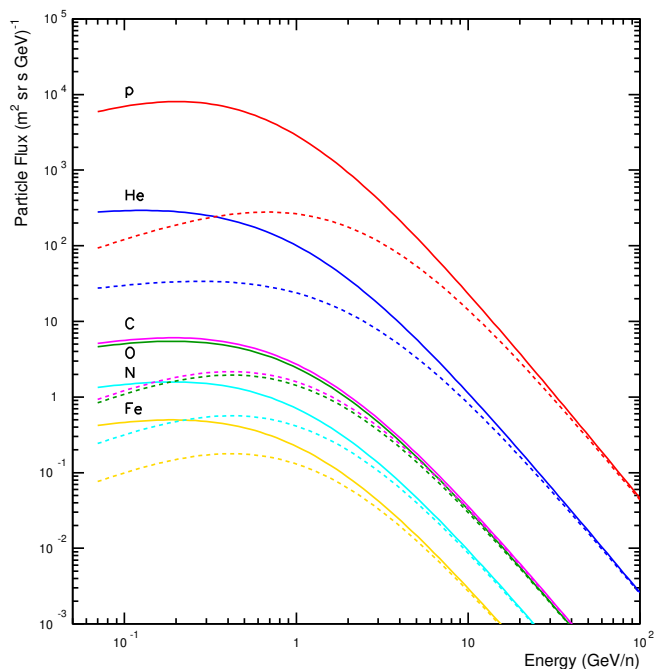


Fig. 3. From top to Bottom panel: proton (p, red), helium (He, blue), carbon (C, magenta), oxygen (O, green), nitrogen (N, cyan) and iron (Fe, yellow) cosmic-ray energy spectra at solar minimum ($\phi= 200$ MV/c; continuous lines) and solar maximum ($\phi= 1200$ MV/c; dashed lines) as extreme conditions for LISA.

onset (December 14, 2016 15:39 UT), for which we considered the undisturbed proton flux measured on November 2006 as suggested in Adriani et al. (2011), at the mid-phase at 17:20 UT and at the deep at 24:00 UT of the same day.

The proton fluxes observed during these events and their parameterization are reported in Figures 5 and 6 and in Table 4 and 5.

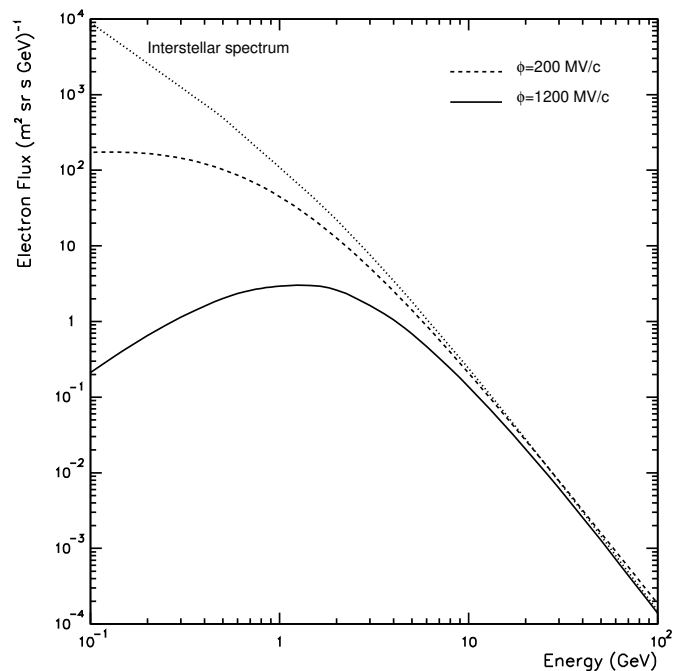


Fig. 4. Galactic electron energy spectra at solar minimum (dashed line) and solar maximum (continuous line) for LISA. The interstellar spectrum is represented by the top dotted line (Moskalenko & Strong 1998).

3.3. Solar energetic particle events during LISA

The charging of the TMs is expected to increase by several orders of magnitude during SEP events (Grimani et al. 2022) with respect to the background values associated with the continuous flow of GCRs. Being sensitive to hadrons above 100 MeV/(n), it is affected by gradual events characterized by proton acceleration above 50 MeV. During the evolution of gradual SEP events, particles show spatial, energy and time variations from onset to decay. At the onset, the solar particle energy spectra most likely show a power-law trend with an exponential cut-off, while at the peak a power-law trend is observed in the majority of cases. The proton spatial distribution is characterized by varying pitch angle distributions. It is worthwhile to recall that the pitch angle is defined as the angle between the particle velocity and the nominal direction of the interplanetary magnetic field Parker spiral. At the onset of the events, the particles mainly propagate along the interplanetary magnetic field lines while during the late phases, the arrival direction becomes isotropic. Since for the LISA simplified geometry we have considered an isotropic matter distribution in the spacecraft, it's not worthy to consider the evolution

Date	A	b	α	β
November 20, 2016	18000	1.115	3.66	0.92
November 21, 2016	18000	1.12	3.66	0.92
November 22, 2016	18000	1.14	3.66	0.92
November 23, 2016	18000	1.159	3.66	0.92
November 24, 2016	18000	1.165	3.66	0.92
November 25-28, 2016	18000	1.172	3.66	0.92
November 29, 2016	18000	1.165	3.66	0.92
November 30, 2016	18000	1.159	3.66	0.92
December 1, 2016	18000	1.156	3.66	0.87
December 2, 2016	18000	1.152	3.66	0.87
December 3, 2016	18000	1.148	3.66	0.87
December 4, 2016	18000	1.14	3.66	0.87

Table 4. Parameterizations of proton energy spectra during a recurrent variation of the proton-dominated flux measured with LPF between November 20, 2016 and December 4, 2016. It is worthwhile to point out that A is measured in protons/(m² sr s GeV^{- α + β +1}), b in GeV while α and β are pure numbers.

Date	A	b	α	β
November 2006 up to December 14, 2006 15:39 UT	18000	1.17	3.66	0.87
December 14, 2006 17:20 UT	18000	1.37	3.66	0.87
December 15, 2006 24:00 UT	18000	1.77	3.66	0.87

Table 5. Parameterizations of proton energy spectra during a Forbush decrease observed on December 14-16, 2006. It is worthwhile to point out that A is measured in protons/(m² sr s GeV^{- α + β +1}), b in GeV while α and β are pure numbers.

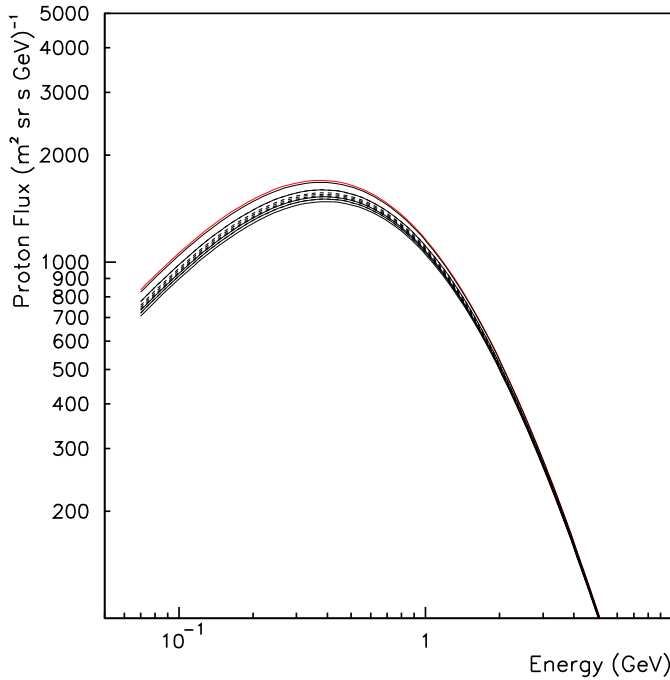


Fig. 5. Recurrent short-term variations of GCRs observed with LPF between November 21, 2016 and December 4, 2016. Continuous lines indicate the decrease phase and the dashed lines the recovery phase. The top red continuous line indicates the proton energy spectrum at the onset of the event.

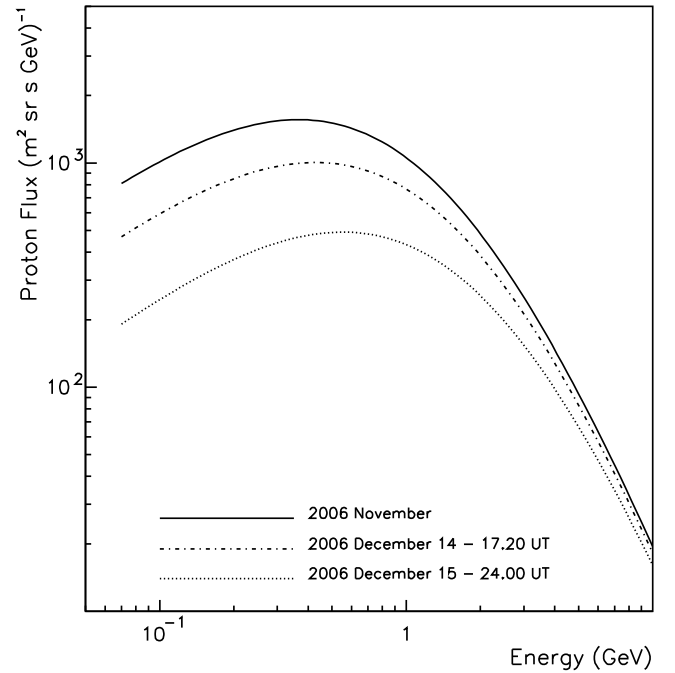


Fig. 6. Forbush decrease observed on December 14-15, 2006 with the PAMELA experiment in space and on Earth with neutron monitors.

of the SEP spatial distribution in the Monte Carlo simulations. The parameterization of the solar particle energy spectra during the event dynamics was discussed for instance in Grimani et al. (2013).

Solar electrons have been demonstrated to play a minor role in affecting the TM charging and won't be detected by the LISA radiation monitors according to the current design (Mazzanti et al. 2023). As a result, even if solar electrons will reach the LISA S/C before protons due to velocity dispersion, no short-term forecasting of SEP events will be allowed on board LISA.

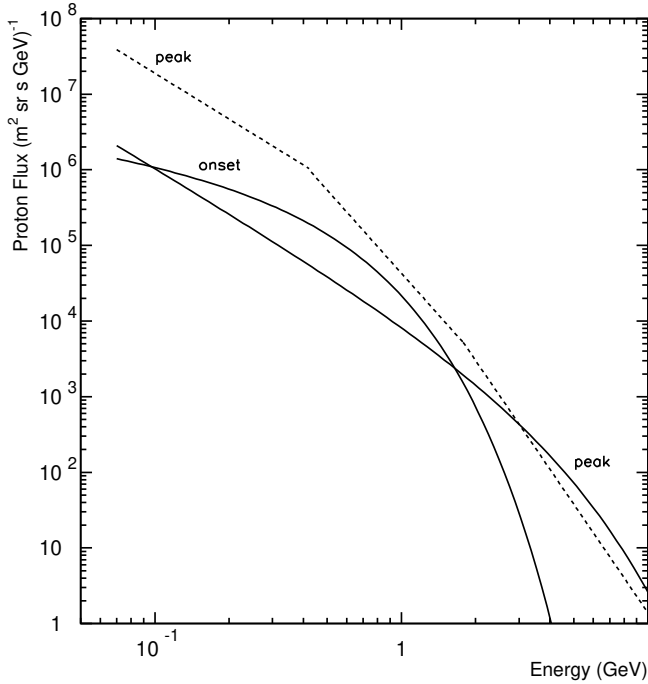


Fig. 7. Solar energetic proton fluxes observed during the evolution of the gradual events dated September 29, 1989 (dashed line) and December 13, 2006 (continuous line). Different phases of the events are indicated. The timings of the events shown in the figure appear in the following in Table 7.

For events that are magnetically well-connected to the active region of the Sun where the solar eruption occurred, the particle flux on board the three LISA satellites can increase by several orders of magnitude in 15 minutes. The average duration of medium-to-strong SEP events (fluence $> 10^6$) is about 1.5 days, although some events can last up to 5 days (Shaul et al. 2006; Rodríguez-Pacheco et al. 2020).

Unfortunately, from the standpoint of the TM charge measurement, during the LPF operations, no SEP events were observed above the GCR background. As a result, for both LPF and LISA the TM charging during SEP events can be only estimated with Monte Carlo simulations (Grimani et al. 2022). The onset and the peak of gradual SEP events of different intensities are considered here. In particular, we study two SEP events of different fluence: the peak of the event dated September 29, 1989 (fluence 10^7 - 10^8 protons cm^{-2} , Miroshnichenko et al. 2000) and the event observed by the PAMELA experiment in space on December 13, 2006 (fluence between 10^6 and 10^7 protons cm^{-2} Adriani et al. 2011). The proton fluxes observed during these events are shown in Figure 7. Data from the Solar Orbiter mission (Müller et al. 2020; García Marirrodriga et al. 2021; Rodríguez-Pacheco et al. 2020)³ on SEP event occurrence above 70 MeV will allow us in the near future to investigate in detail the effects of several other event dynamics on LISA.

We stress that SEP events with fluences of 10^5 - 10^6 protons cm^{-2} are not observed at solar minimum above the background of GCRs above 70 MeV.

On the basis of observations gathered during the past solar cycles, the expected number of SEP events during the LISA operations can be at most of the order of 10 per year during the

first part of the mission since the LISA launch is scheduled at the maximum of the solar cycle 26 (Singh & Bhargawa 2019).

4. LISA Test Mass charging case studies

In space, the deposit of a charge on the TM is an inherently Poissonian process. Each deposit j , say one elementary charge or more, of either signs, has its rate λ_j . The TM charges up with a rate:

$$\lambda_{NET} = \sum_{j=-\infty}^{+\infty} j \lambda_j \quad (\text{s}^{-1}), \quad (4)$$

This charging process produces on the TM shot noise $S_Q = 2eI$ with the current $I = \lambda_{EFF}e$, where:

$$\lambda_{EFF} = \sum_{j=-\infty}^{+\infty} j^2 \lambda_j \quad (\text{s}^{-1}). \quad (5)$$

The integral of the charging yields the "red" power spectral density of the deposited charge $S_Q = 2\lambda_{EFF}e^2/(2\pi f)^2$, as a function of the frequency f (Araújo et al. 2005).

The LISA observatory measures the relative motion of TM pairs in the 0.1 mHz to 1 Hz band (Amaro-Seoane et al. 2017; Colpi et al. 2024). Therefore, the calculation of the λ_{NET} and λ_{EFF} must be representative at time scales of 1000s seconds or more for the galactic cosmic-ray flux.

Figure 8 illustrates the evolution of λ_{NET} and λ_{EFF} as a function of the simulation time, for the proton flux at solar minimum ($\phi = 200$ MV). The error bars on the figure represent the statistical uncertainty on the results. As expected, the uncertainties on λ_{NET} decrease uniformly with simulation time, while showing an irregular trend on λ_{EFF} . This is due to the fact that, given the quadratic dependence of the latter on the deposited charge, the occurrence of events with high charging (large deposits) has a more marked relevance on the evaluation of the uncertainty. Both λ_{NET} and λ_{EFF} show an increasing trend, saturating to a constant value above ~ 100 second simulation time. This is expected: because of the power-law cosmic-ray spectral shape, not enough high-energy (>10 GeV/n) particles are simulated for low simulation times. These high-energy particles are more likely to be associated with a large production of secondaries deposited on the TMs. We fitted the λ_{NET} and λ_{EFF} trends with an asymptotic exponential function, obtaining the results shown in the same Figure, where the asymptote (A) represents the expected value of the two parameters. From the figure it is clear that a good convergence of the results, especially for λ_{EFF} , can be obtained only with simulation times above 10^3 sec for protons. We set conservatively to 10^4 s the simulation time for protons at both solar minimum and maximum. This minimum simulation time was further increased for rare particles in cosmic rays such as nuclei and electrons. The simulation time used for the various species are reported in the second column of Table 6.

In the top panel of Figure 9, as an example, we have reported the contributions to λ_{NET} and λ_{EFF} as a function of the energy of primary protons at solar minimum. The λ_{NET} decreases abruptly above 1 GeV. The meaning of this sharp decrease can be inferred by observing the break-down of the contribution of the different secondary particle species generated by the interaction of the primary protons appearing in the bottom panel of the same figure. Below 200 MeV the λ_{NET} is dominated by protons, stopping in the TM. The production of positive and negative charged pions

³ <https://soar.esac.esa.int/soar/>

Primary Particle	Sim. time [s]	Solar minimum				Solar maximum			
		λ_{NET} [s ⁻¹]	error [s ⁻¹]	λ_{EFF} [s ⁻¹]	error [s ⁻¹]	λ_{NET} [s ⁻¹]	error [s ⁻¹]	λ_{EFF} [s ⁻¹]	error [s ⁻¹]
Protons	10000	51.50	0.80	440.5	8.79	4.30	0.14	154.70	15.50
Helium	50000	5.60	0.20	77.00	2.10	1.05	0.05	53.30	7.39
Carbon	50000	0.50	0.10	17.50	1.10	0.12	0.01	6.50	0.10
Nitrogen	50000	0.25	0.05	2.0	0.1	0.12	0.01	0.5	0.01
Oxygen	50000	0.30	0.05	14.50	2.00	0.13	0.01	8.18	0.49
Iron	150000	0.20	0.02	30.50	2.50	0.05	0.01	15.60	2.30
electrons	100000	-0.50	0.05	69.05	1.70	1.00	0.02	28.90	1.85
Total	-	57.85	0.83	651.05	9.80	6.77	0.15	267.70	17.40

Table 6. Monte Carlo estimates of λ_{NET} and λ_{EFF} for the different species of the GCR particles during $\phi = 200$ MV (Solar Minimum) and $\phi = 1200$ MV (Solar Maximum) conditions.

Date	Event	Phase	λ_{NET} [s ⁻¹]	error [s ⁻¹]	λ_{EFF} [s ⁻¹]	error [s ⁻¹]
14:12 UT Sept 29, 1989	SEP	Peak	13414	75	40912	1781
03:18 UT Dec 13, 2006	SEP	Onset	2351	50	6038	270
04:33 UT Dec 13, 2006	SEP	Peak	1037	35	2519	110
15:39 UT Dec 14, 2006	FD	Onset	13.6	0.5	262	55
17:20 UT Dec 14, 2006	FD	Mid-Phase	9.8	0.3	187	16
00:00 UT Dec 15, 2006	FD	Dip-Phase	6.1	0.2	163	17

Table 7. Monte Carlo estimates of λ_{NET} and λ_{EFF} for proton fluxes under non-recurrent transient solar events.

Particle	Solar minimum		Solar maximum	
	λ_{NET} [s ⁻¹]	λ_{EFF} [s ⁻¹]	λ_{NET} [s ⁻¹]	λ_{EFF} [s ⁻¹]
Protons	48.7	672.1	14.1	255.9
Helium	15.0	289.8	4.1	183.1
Carbon	1.4	93.9	0.8	57.5
Nitrogen	0.4	26.9	0.2	21.1
Oxygen	1.7	123.9	0.9	64.6
Iron	0.4	72.8	0.3	63.3
electrons	-3.2	216.7	-0.1	91.1
Total	64.4	1496.1	20.3	737.6

Table 8. FLUKA/LEI Monte Carlo estimates of λ_{NET} and λ_{EFF} for different species of GCR particles during $\phi = 200$ MV and $\phi = 1200$ MV solar conditions (Villani et al. 2024a).

Date	Phase	λ_{NET} [s ⁻¹]	λ_{EFF} [s ⁻¹]
December 13, 2006	ONSET	2425	5695
December 13, 2006	PEAK	1123	2360
September 29, 1989	PEAK	16358	56733

Table 9. FLUKA/LEI Monte Carlo estimates of λ_{NET} and λ_{EFF} for proton fluxes during SEP events.

(shown in the figure) above this energy tags the occurrence of hadronic interactions in the body of the TM (minimum traversed

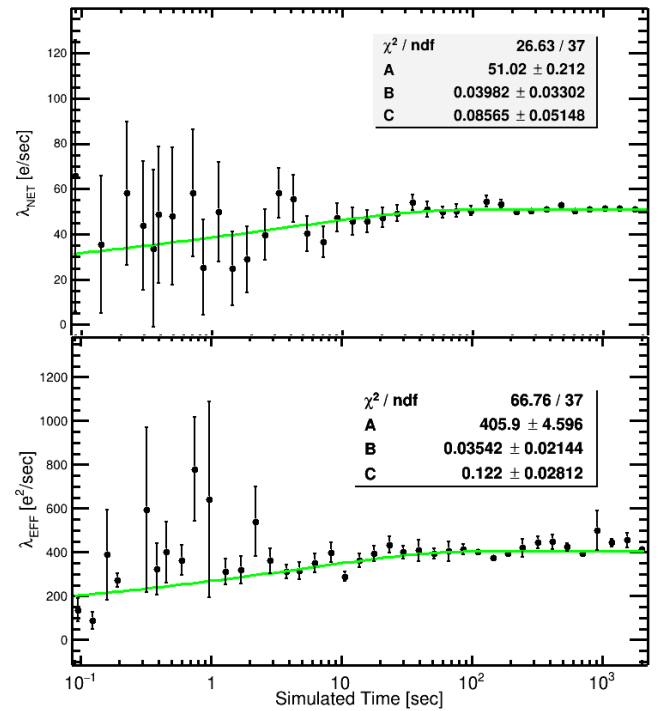


Fig. 8. Evolution of λ_{NET} and λ_{EFF} over simulation time for the proton energy spectrum at solar minimum ($\phi = 200$ MV). Error bars indicate statistical uncertainty. The green line represents an exponential fit to data to show the trend $(A(1-e^{-Bt})^C)$.

gold material grammage 91 g cm^{-2}). The secondary particles es-

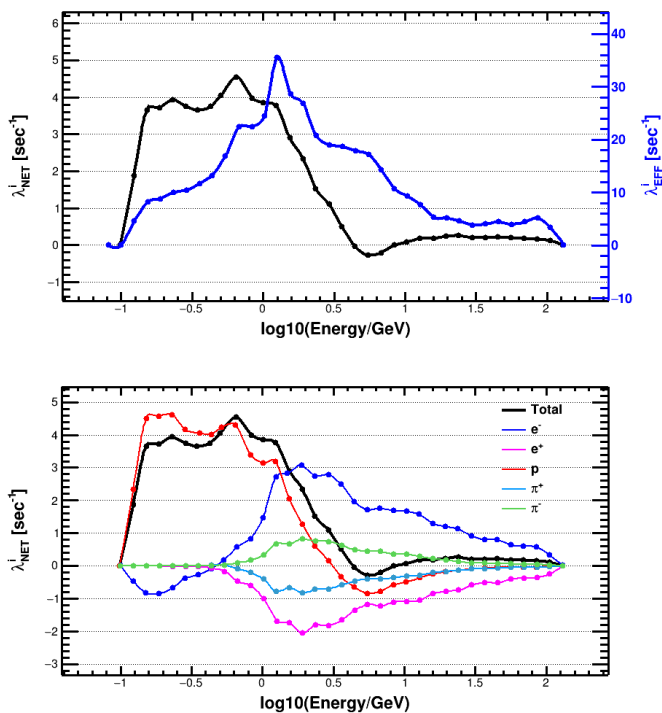


Fig. 9. Top panel: Comparison of the contribution to total λ_{NET} and to total λ_{EFF} for a primary proton flux ($\phi = 200$ MV) and particles of different energies. Bottom panel: Break down of the λ_{NET}^i from the most abundant particle species contributing to the total λ_{NET} as a function of the energy of the primary proton.

cape the TM in a larger number with respect to those penetrating from outside: escaping negative charged particles charge positively the TM, the opposite occurs for positively charged particles. However, the electron curve is also affected by an extra production of electrons by particle ionization. It is worthwhile to point out that globally positive and negative pions, electrons and positrons give a negligible contribution to the total charging with respect to protons.

The trend of λ_{EFF} as a function of the primary proton energy shows contributions peaking for primary proton energies in the GeV range and with significant contributions spanning from 150 MeV to 50 GeV (see Figure 9). Charge deposits of opposite signs sum up quadratically in the λ_{EFF} formula (Eqn. 5) and do not cancel out.

The discussions reported above, allowed us to set properly the simulation timeframe for all particle species sensibly contributing to the TM charging as discussed in Section 3. As an example of TM charging timeseries, we report in Figure 10 the Monte Carlo simulation results obtained for primary protons and iron nuclei under the same solar modulation conditions ($\phi=200$ MV). Both timeseries exhibit a prevalence of positive charge deposits reaching values of several hundreds of elementary charges per second deposited on the TM. As expected, these events are significantly more frequent in the iron case, due to the overall amount of electrons generated by ionization which scales with the square of the particle charge.

This evidence emerges more clearly in the *charging histograms*⁴, shown in the right panel of the same figure, where one can notice that the occurrence of large charge deposits is consistently higher for the iron nuclei.

⁴ Events with 0 deposit are not included in the charging histograms

Figure 11 (top panel) presents a comparison between the charging histograms obtained from two proton simulations at extreme solar minimum ($\phi = 200$ MV) and solar maximum ($\phi = 1200$ MV) conditions. The deposit rates (see top panel of Figure 11) are consistently lower for solar maximum fluxes. This imbalance fades out for higher and higher charge deposits since solar maximum fluxes are relatively poor in low-energy particles with respect to solar minimum fluxes.

A global charging histogram from a complete GCR flux simulation of 10000 seconds at extreme solar minimum ($\phi = 200$ MV) is presented in Figure 11 (bottom panel), broken down by contributions from each simulated particle species. Only species with the highest expected contributions were simulated, using the flux parametrization discussed in Section 3. As can be seen, the peak of the distribution, which is mostly determining the net charging, is dominated by proton and helium contributions, while the tails, mostly affecting λ_{EFF} are populated by other particle species in a more than proportional way with respect to their relative abundance.

The results regarding the λ_{NET} , λ_{EFF} and their respective uncertainties obtained with TMCTK in different space environment conditions and for different particles are reported in Tables 6. From this table it appears clear that the dominant contribution to the total λ_{NET} and λ_{EFF} is due to primary protons. The contribution of nuclei is in general smaller, but relatively important with respect to the abundance of these particles in GCRs. This is particularly evident for iron nuclei, which give a contribution of $\sim 10\%$ to the total λ_{EFF} due to the combined effects of its high Z and relative abundance with respect to other heavy nuclei. Also electrons, constituting only 2% of the CGR sample, give a $\sim 10\%$ contribution to the total effective charging. Moreover, it is the only particle species showing a marginally negative contribution to λ_{NET} .

In Figure 12 (top and bottom panel) and Table 7, we present the time evolution of λ_{NET} and λ_{EFF} for the recurrent short term variation appearing in Figure 5 and for the non-recurrent shown in Figure 6. In Table 7 we have reported also the results on the simulation of two SEP events dated September 29, 1989 and December 13, 2006 (see Figure 7). For SEP events, we carried out simulations for a fixed duration of 6 seconds given their rapid evolution and their extremely high flux with respect to GCRs. Figure 12 (middle panel) shows also the time evolution of λ_{NET} and λ_{EFF} for the December 13, 2006 SEP. The λ_{NET} appears to follow the variations of the input fluxes being dominated by the primaries stopping inside the TM. This correlation is less evident for λ_{EFF} , which is more influenced by events producing a large number of secondary particles.

5. Discussion of results

The results of the charge rate λ_{NET} from protons in Table 6 appear in relatively good agreement with those presented in Armano et al. (2023) obtained with a Monte Carlo simulation using GEANT4 version 10.3 (without the DNA module), where the ionization is treated using Opt4 physics, and the LEE production from electrons and hadrons is managed with a yield-based approach. In Armano et al. (2023) the net charging for the LPF TM was calculated on the basis of the INTEGRAL mission measurements by considering the minimum of the solar cycles 23 and the maximum of the solar cycle 24: the estimates for λ_{NET} range from $+8 \text{ s}^{-1}$ to $+40 \text{ s}^{-1}$, whereas we find $+4 \text{ s}^{-1}$ to $+51 \text{ s}^{-1}$ under extreme conditions of solar maximum and solar minimum (see Table 6). With the same Monte Carlo, Wass et al. (2023) estimated a $\lambda_{NET} = 29.3 \text{ s}^{-1}$ and a $\lambda_{EFF} = 390 \text{ s}^{-1}$ for

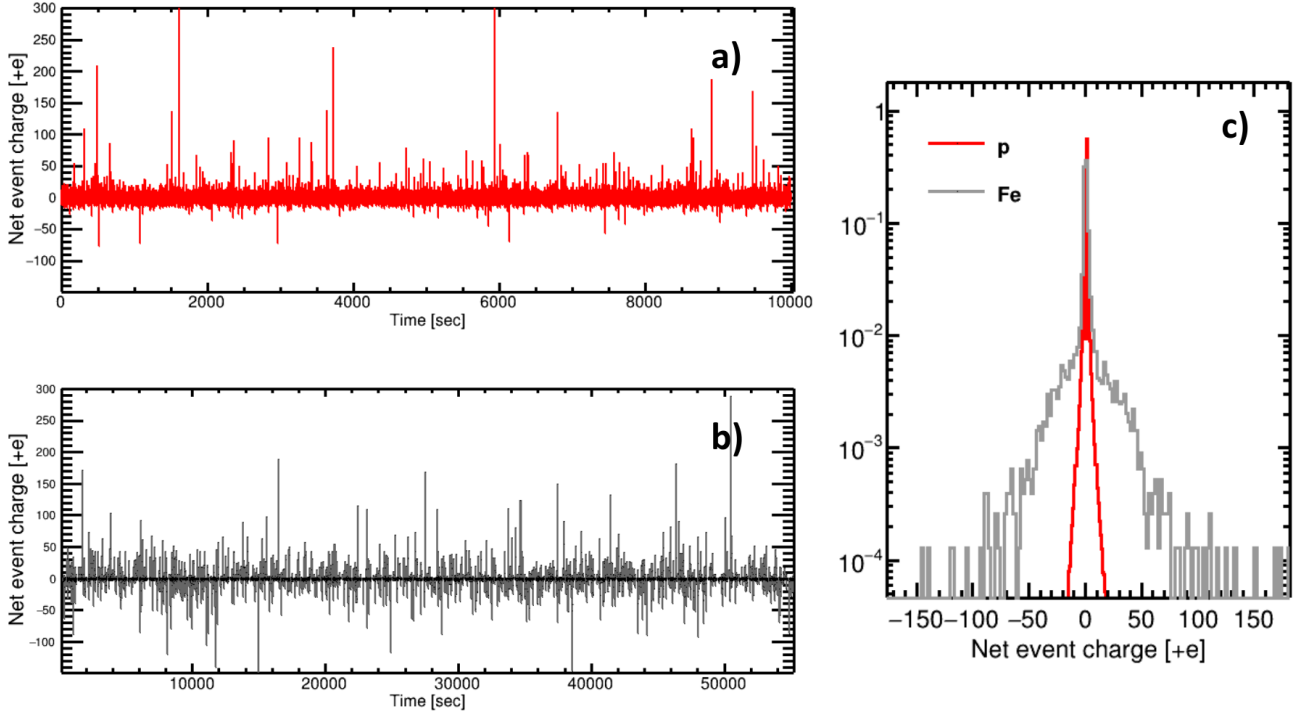


Fig. 10. Comparison of charging time series for proton (a) and iron nuclei (b) fluxes at $\Phi = 200$ MV. Panel (c) shows a comparison between the charging histograms of the two time series normalized to the number of events.

the proton flux in June 2017. In the same solar modulation condition, the proton flux simulated with our Toolkit returns a result of $\lambda_{NET} = 31.0 \pm 1.0 \text{ s}^{-1}$ and $\lambda_{EFF} = 375 \pm 14 \text{ s}^{-1}$ with an exceptional agreement despite the different spacecraft geometries considered in the simulations. The consistency of the two GEANT4 Monte Carlo is also confirmed by the results of the simulation of the TM environmental charging evolution as a function of the TM potential shown in Figure 13. The data points in the Figure were calculated using the Multiphysics software COMSOL propagating the low energy electrons in the electric field calculated for various TM potential. We recall that in LPF we noticed that the TM charge rate depended on the TM potential: the rate approached zero (TM equilibrium potential) for $V_{TM} \approx 0.9$ V, very close to the value calculated by Wass et al. (2023) and that found by our simulation (see Figure 13). We note that this was one of the main argument in favor of the presence of low energy electrons in the gap between the TM and the EH and for including in the old versions of the Monte Carlo the physics of the low energy electrons.

Despite all this, our Monte Carlo simulation toolkit still needs improvements. The comparison of the results reported in the Tables 6, 7, and 8 shows that while the net charging results are similar for GEANT4 and FLUKA/LEI calculations, the effective charging in FLUKA/LEI appears, on average, higher by a factor of 2 and in a better agreement with the observations gathered on board LPF (Armano et al. 2017; Grimani et al. 2022). It is worthwhile to stress that this discrepancy is much more evident with GCRs with respect to SEPs, due to a more relevant production of secondary electrons (see Grimani et al. 2022, and Fig.7).

We have investigated the possible origin of the discrepancies between FLUKA/LEI and TMCTK. Part of the difference in the results could be due to the spacecraft geometry (FLUKA/LEI

uses a realistic reproduction of LPF geometry). Nevertheless, as stated before, we studied the dependence of TMCTK results on the material distribution around the TMs: we changed the shell material amount and/or their radius finding no relevant differences.

The main difference between FLUKA/LEI and GEANT4-DNA is ascribable to a much larger number of secondary electrons surrounding the test masses in FLUKA/LEI. In the Introduction we stressed that the hadrons ionization in GEANT4 presents a sharp cut-off at the average ionization potential in gold of 790 eV, while in FLUKA/LEI the implementation is carried out down to 10 eV. Moreover, a simple experiment was carried out to compare the performance of the two tools with primary electrons. We simulated a beam of 10 keV electrons crossing 100 nm thick gold slab. In Figure 14 we compare the spectrum of secondary electrons per incident particle transmitted by the target: the spectrum associated with the GEANT4-DNA simulation exhibits a marked excess at a few eV and appears approximately one order of magnitude below the LEI outcome, in particular below 1 keV. Moreover, the GEANT4-DNA spectrum shows sharp step variations, typical of discontinuous parameterizations of cross sections and/or electron mean free path in the 10–100 eV energy interval.

6. Impact on LISA sensitivity

In the previous sections we have discussed the LISA TM charging due to the action of particle fluxes of galactic and solar origin. We now analyse the impact of the charging process on the LISA mission performance. The LISA TM is subjected to a Coulomb force due to the interaction of the TM charge with any non-zero average electrostatic field, from non-uniform surface "patch potentials" (Antonucci et al. 2012) and/or any ap-

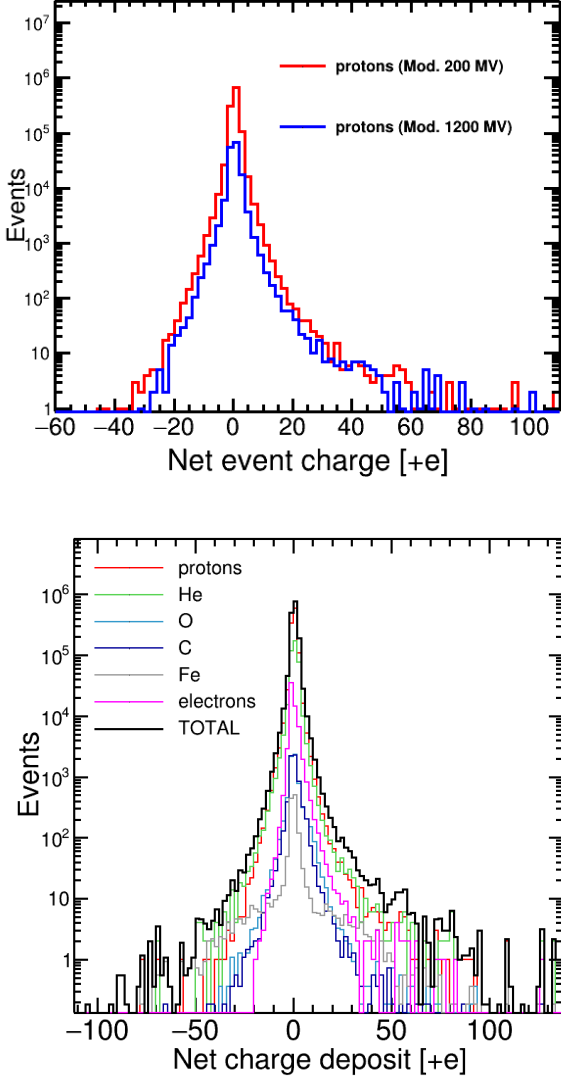


Fig. 11. Top panel: Comparison of charging histograms obtained from simulations of proton fluxes at extreme solar minimum ($\Phi = 200$ MV) and solar maximum ($\Phi = 1200$ MV) conditions. Bottom panel: Total charging histogram obtained from complete simulation of CR flux (10000 seconds) at solar minimum condition ($\Phi=200$ MV), broken down in its contributions from every simulated CR specie.

plied fields. The formula for the force along the LISA sensitive axis, F_x , is:

$$F_x = Q_{TM}E_x = Q_{TM} \frac{\delta C_x}{\delta x} \frac{\Delta_x}{C_{TOT}}, \quad (6)$$

where the electric field x -component E_x is expressed in terms of the x -electrode derivative $\frac{\delta C_x}{\delta x} \approx 300$ pF/m, the TM self capacitance $C_{TOT} \approx 34$ pF, and the DC bias voltage Δ_x normalize the stray electrostatic field component along the x axis to an electrostatic potential applied to a single x -face GRS electrode (Antonucci et al. 2011b; Antonucci et al. 2012). A charge event occurring due to GCR flux short term variations or SEPs, makes Q_{TM} changing with time producing a force signal. The time shape of the force is entangled to the time characteristics and to the energy content of the charge event. We have seen in Section 4 that we are able to reconstruct the evolution of the charging signal (see for example Figure 8), by using Monte Carlo simu-

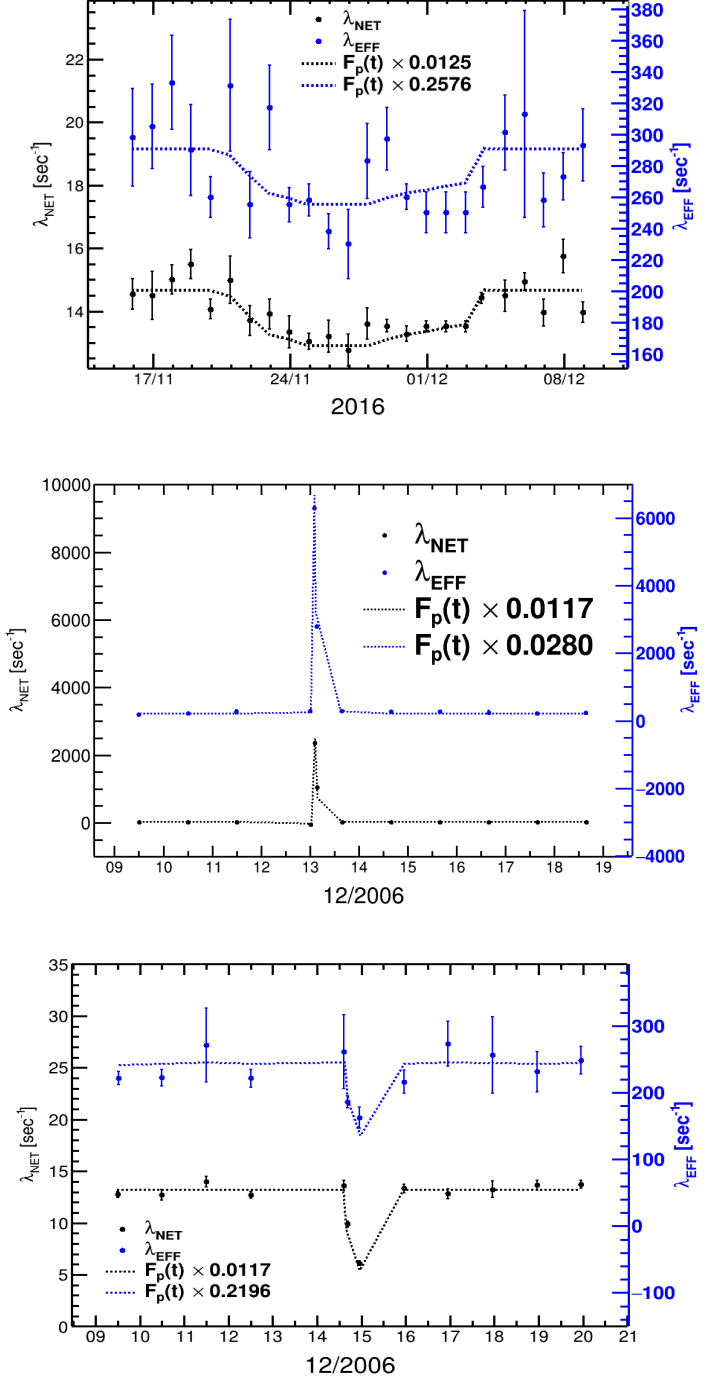


Fig. 12. Top panel: Net (black points) and effective (blue points) charging of the LISA TM during the recurrent GCR variation associated with the passage of one high-speed solar wind stream observed with LPF in November 2016. Only the proton flux was simulated. As a comparison, the trend of the simulated proton flux $F_p(t)$, integrated in the 0.5-1.5 GV rigidity bin, was superimposed to the λ_{NET} and λ_{EFF} data through multiplication by a constant (dashed lines). Central panel: Net (black points) and effective (blue points) charging of the LISA TM during the SEP event of December 13, 2006. The dashed lines show the same comparison of the top panel with the normalized proton flux. Bottom panel: Net (black points) and effective (blue points) charging of the LISA TM during the Forbush decrease following to the SEP event of December 13, 2006 (SEPs were subtracted from data). The dashed lines show the same comparison of the top panel with the normalized proton flux.

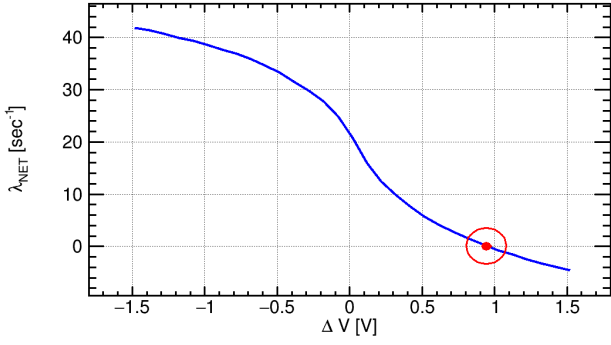


Fig. 13. Simulation of the TM net charging evolution as a function of the TM to EH ground electric potential for a proton flux corresponding to the initial operation timeframe of LPF.

lations of the different temporal phases of the event. From that, the force timeseries can be calculated according to Eqn. 6. DC bias $\Delta_x \approx 100$ mV has been observed in LISA-like GRS and electrostatically compensated to $\Delta_x = 5$ mV level in laboratory and during LPF flight operations (Antonucci et al. 2012; Armano et al. 2017). We assumed $\Delta_x = 5$ mV, the expected value during LISA science operations.

Figures 15 and 16 show the evolution of the induced force on the LISA test masses for the event of December, 13-15 2006, including SEP and FD. The dynamics of the Forbush decrease was reconstructed as described in Sect. 3 and shown in Figure 6. The flare associated with the December 13, 2006 SEP event was observed at 02:14 UT from the active region NOAA 10930. A coronal mass ejections accelerating protons observed with PAMELA between 03:18 UT and 03:49 UT was detected by LASCO at 02:54, thus revealing a very good magnetic connection between the active region and the PAMELA satellite. The time lag between onset, peak and decay phases of the SEP event are set on the basis of proton flux measurements carried out with PAMELA (see Figure 7 and Adriani et al. (2011)).

For LISA performance, it is interesting to calculate the signal-to-noise ratio (SNR) of the charging events:

$$(SNR)^2 = \int_{f_{min}}^{\infty} \frac{|FFT(F_x)|^2}{S_n} df, \quad (7)$$

with $f_{min} = 20 \mu\text{Hz}$ and $S_n \approx 4S_g \left(1 + \left(\frac{0.4\text{mHz}}{f}\right)^2\right) \left(1 + \left(\frac{f}{8\text{mHz}}\right)^2\right)$ (see Figure 17) expressing the low frequency limit of the LISA noise sensitivity for the X-Michelson Time Delay Interferometry (TDI, Tinto & Armstrong 1999; Muratore et al. 2023) combination in terms of the residual force noise on a single TM⁵, where $S_g^{1/2} = 3 \text{ fm s}^{-2} \text{ Hz}^{-1/2}$ (Armano et al. 2018b; Quang Nam et al. 2023; Colpi et al. 2024). At these frequencies the observatory sensitivity is completely dominated by TM acceleration noise, as so we neglect the interferometry noise contribution in this calculation (Muratore 2023). The SNR calculation yields 0.1 and 20 for the FD and the SEP event, respectively, indicating that LISA will be able to clearly observe the solar event. Were DC biases Δ_x larger than the 5 mV limit because of lack of compensation, also Forbush decreases could pollute LISA data.

In that calculation, we have neglected the effect of the charge control system present in LISA, with the expectation that the

⁵ The factor 4 multiplying S_g accounts for the contribution of the four TMs involved in the Michelson interferometer.

response time of a possible continuous discharge will be slow enough, of order 10^5 seconds, to not have a large impact on "filtering" the SEP charge dynamics in the LISA band above 10^{-4} Hz. As such, the SNR should not be much different in the case of continuous or intermittent discharge.

We recall that the rate of SEP events with particle acceleration above tens of MeV is of the order of ten per year, at least for the transfer phase of the LISA satellites and the mission commissioning phase; the rate decreases to 8.5 at the beginning of the science data-taking period to about 1 at the end of the nominal LISA observation time (Grimani et al. 2025). The capability to discriminate these spurious events with respect to some gravitational ones lays on on-board measurements of the satellite radiation monitors and on the Monte Carlo simulations that would allow for reconstructing the event and inform the analysis of LISA data (Quang Nam et al. 2023). Additionally it would be possible to continuously monitor the TM charge such as to allow possible subtraction of the force disturbance from the observatory TDI time series.

Ultimately, it is worth to note that from Eqn. 6, fluctuations on the TM charging process, here accounted with the λ_{EFF} parameter, would generate force noise on the TM. Although our simulation have shown some limit in reproducing LPF measurements, we can use FLUKA/LEI results, as those shown in Tables 8 and 9 to conclude that under GCR flux λ_{EFF} won't exceed 1500 s^{-1} . This number appears close to what LPF has measured (see Table 1) and would yield acceleration noise $S_a^{1/2} = \frac{\sqrt{2e^2\lambda_{EFF}}}{2\pi M_{TM} 10^{-4}\text{Hz}} \frac{\delta C_x}{\delta x} \frac{\Delta_x}{C_{TOT}} \approx 0.3 \text{ fm s}^{-2} \text{ Hz}^{-1/2}$ comfortably within $3 \text{ fm s}^{-2} \text{ Hz}^{-1/2}$ allowed in LISA for stray electrostatic forces at 0.1 mHz , the lower end of the LISA measurement bandwidth.

In SEP events, together with the net charge λ_{NET} , also the charge fluctuation λ_{EFF} rises largely, reaching values up to $6 \times 10^3 \text{ s}^{-1}$ for medium strong event such that on 13 Dec. 2006, or even $6 \times 10^4 \text{ s}^{-1}$ for the strong event on 29th Sept 1989 (see Table 7 and 9). For SEP event of longer timescales (3-5 days), the analysis of the impact of such event in LISA becomes more complicated. Several aspects should be in particular taken into account: what discharge control algorithm will be in use, what ability we will have in flight to adjust its parameters, what will be the equilibrium potential at which the TM would rise. We leave this study for a dedicated paper.

7. Conclusions

This work presents a toolkit for the estimation of the effects of the space environment on the charging of LISA TM. The toolkit is based on GEANT4 package with GEANT4-DNA module for the generation and the propagation of the secondary electrons with energies below 100 eV in the outer 150 nm of the gold plated layers of the TM and EH. Low-energy electrons have been found to play a key role in the TM charging from the comparison of experimental data gathered with LPF and pre-launch Monte Carlo simulations. The adoption of the DNA module with its more accurate simulation of very low energy electrons, returned a better agreement with LPF experimental data in line with other GEANT4 implementations of low-energy electromagnetic physics. Despite that, about a factor of two mismatch remains in the estimate of the charging noise (and thus of λ_{EFF}) with respect to the LPF data. The good agreement between the outcomes of the FLUKA/LEI Monte Carlo and the LPF data suggests that DNA module presents a still incomplete description of the role of LEE in the TM charging process. This is confirmed from the comparison of FLUKA/LEI and GEANT4-DNA of the

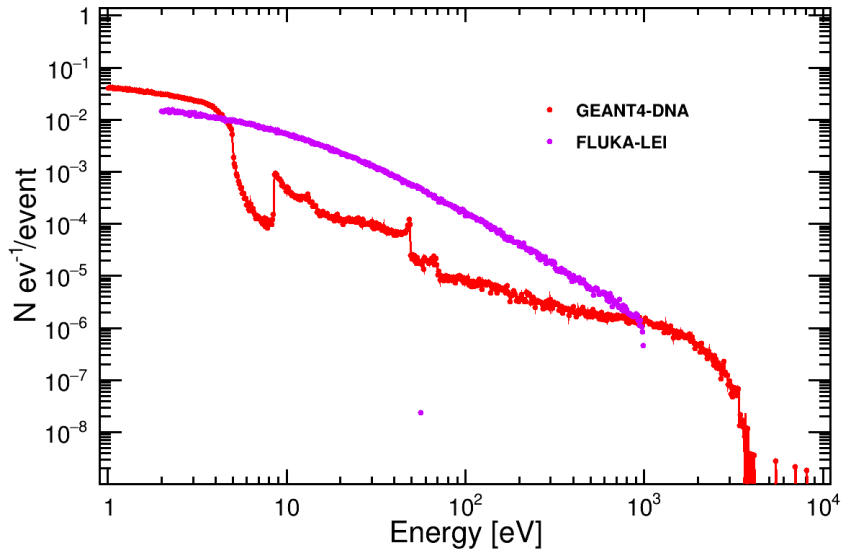


Fig. 14. Comparison between the energy spectra of secondary electrons per incident primary electron transmitted by a 150 nm thick gold target simulated using GEANT4-DNA (red curve) and LEI (purple curve).

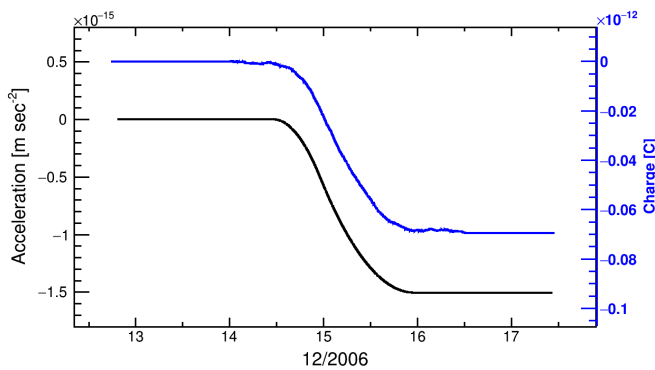


Fig. 15. Forbush decrease contribution to the TM accumulated charge (blue line) and to TM acceleration (black line).

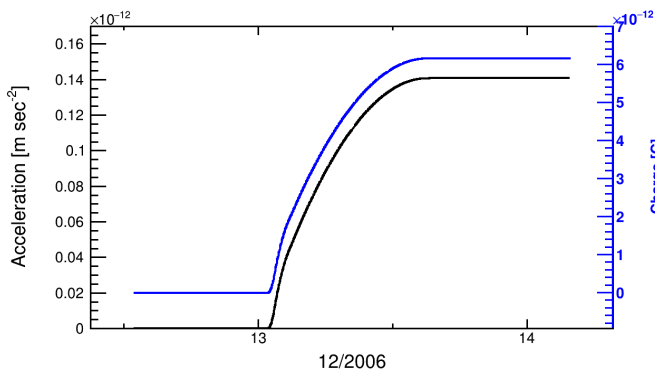


Fig. 16. SEP contribution to the TM accumulated charge (blue line) and to TM acceleration (black line).

energy spectra of simulated electrons emitted from a 100 nm gold layer with incident electrons beams of 10 keV energy. This issue was acknowledged by scientists of the GEANT-4 collabo-

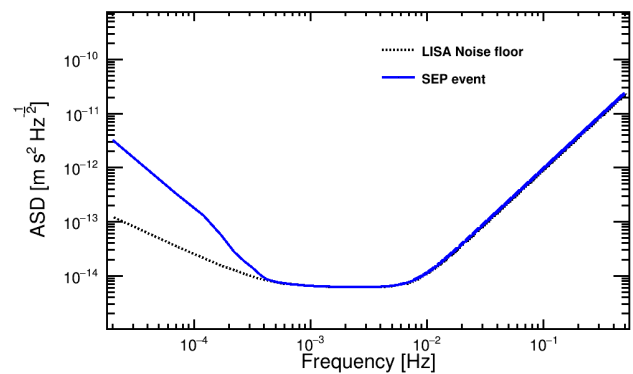


Fig. 17. Amplitude spectral density of the LISA force noise and the SEP force signal in a time window of 2×10^5 seconds.

ration and improvements are expected in the future release of the DNA module for low-energy electromagnetic physics in gold. It is important to stress that with respect to the TM net charging (λ_{NET}) estimates, GEANT4 and FLUKA/LEI Monte Carlo appear consistent with each other and in good agreement with LPF measurements.

We have used the toolkit to consider different case studies associated with the impact of the environment on the LISA mission. In particular, we have evaluated the TM charging due to GCRs under extreme solar modulation conditions, during recurrent and non-recurrent short-term variations of the GCR flux and during SEP events of different intensity. By extrapolating the acceleration noise budget of LPF TM to LISA, the TM charging due to GCRs for the extreme cases of solar activity is well below the $3 \text{ fm s}^{-2} \text{ Hz}^{-1/2}$ total acceleration noise requirement. LISA will be a signal dominated mission, short-term variations of incident particle fluxes may generate spurious signals mimicking genuine GWs. Whereas GCR recurrent short-term variations, having typical durations of 9.1 days, are completely out

of the LISA sensitivity band, the sharp decrease observed during FDs (see Figure 15) generates a step-like signal that would appear in the LISA band. This signal could have $\text{SNR} > 1$ with large stray electrostatic fields, $\Delta_x \geq 50$ mV, within the few mm gap between EH and TM.

SEP events have shown to produce increases of several orders of magnitude on net charging and charge noise over typical time scales from a few hours to a five days depending on the magnetic connection of the spacecraft to an active region of the Sun from which several events are generated in a row. We have found that a medium-strong event of duration of a few hours, such as that measured by PAMELA in Dec. 2006, could generate a strong $\text{SNR} \approx 20$ signal in the LISA band, which could require vetoing the relevant portions of the datastream.

In addition to spurious signal generation, SEP events with longer time scales may charge the TM to potentials as large as 1 V affecting the mission operation. Therefore, for LISA it will be important to analyse also the response of the charge management system to these events.

Acknowledgements. The authors thank E. Castelli (NASA) for helpful discussions, suggestions and simulations regarding the impact of the charging signal to the LISA sensitivity. This work was funded under the European Space Agency contract No. 4000133571/20/NL/CRS - TEST MASS CHARGING TOOLKIT AND LPF LESSONS LEARNED. F. Dimiccoli and V. Ferroni were funded by ASI - Agenzia Spaziale Italiana - ACCORDO ATTUATIVO n. 2024-36-HH.0 dell'ACCORDO QUADRO ASI/Università di Trento n. 2017-32-H.0 - Addendum n.2017-29-H.1-2020 All'Accordo n. 2017-29-H.0

References

- Abbott, B. P., Abbott, R., Abbott, T. D., et al. 2016, *Phys. Rev. Lett.*, 116, 061102
- Adriani, O., Barbarino, G. C., Bazilevskaya, G. A., et al. 2011, *ApJ*, 742, 102
- Agostinelli, S. et al. 2003, *Nucl. Instrum. Meth. A*, 506, 250
- Aguilar, M., Cavazonza, L. A., Ambrosi, G., et al. 2021, *Phys. Rev. Lett.*, 127, 271102
- Allison, J., Amako, K., Apostolakis, J., et al. 2006, *IEEE Transactions on Nuclear Science*, 53, 270
- Allison, J. et al. 2016, *Nucl. Instrum. Meth. A*, 835, 186
- Amaro-Seoane, P., Audley, H., Babak, S., et al. 2017, arXiv e-prints, arXiv:1702.00786
- Antonucci, F., Armano, M., Audley, H., et al. 2011a, *Classical and Quantum Gravity*, 28, 094002
- Antonucci, F., Armano, M., Audley, H., et al. 2011b, *CQG*, 28, 094001
- Antonucci, F., Armano, M., Audley, H., et al. 2012, *CQG*, 29, 124014
- Antonucci, F., Cavalleri, A., Dolesi, R., et al. 2012, *Phys. Rev. Lett.*, 108, 181101
- Araújo, H., Wass, P., Shaul, D., Rochester, G., & Sumner, T. 2005, *Astroparticle Physics*, 22, 451
- Armano, M., Audley, H., Auger, G., et al. 2016, *Phys. Rev. Lett.*, 116, 231101
- Armano, M., Audley, H., Auger, G., et al. 2017, *Phys. Rev. Lett.*, 118, 171101
- Armano, M., Audley, H., Auger, G., et al. 2017, *Phys. Rev. Lett.*, 118, 171101
- Armano, M., Audley, H., Baird, J., et al. 2018a, *Astrophys. J.*, 854, 113
- Armano, M., Audley, H., Baird, J., et al. 2019, *Astrophys. J.*, 874, 167
- Armano, M., Audley, H., Baird, J., et al. 2023, *Phys. Rev. D*, 107, 062007
- Armano, M., Audley, H., Baird, J., et al. 2018b, *Phys. Rev. Lett.*, 120, 061101
- Battistoni, G., Boehlen, T., Cerutti, F., et al. 2014, in *Joint International Conference on Supercomputing in Nuclear Applications + Monte Carlo*, 06005
- Bernal, M. A., Bordage, M. C., Brown, J. M. C., et al. 2015, *Physica Medica*, 31, 861
- Böhlen, T. T., Cerutti, F., Chin, M. P. W., et al. 2014, *Nuclear Data Sheets*, 120, 211
- Burger, R. A., Potgieter, M. S., & Heber, B. 2000, *Journal of Geophysical Research: Space Physics*, 105, 27447
- Colpi, M., Danzmann, K., Hewitson, M., et al. 2024, arXiv e-prints, arXiv:2402.07571
- Cucinotta, F. A., Katz, R., Wilson, J. W., & Dubey, R. R. 1996, in *American Institute of Physics Conference Series*, Vol. 362, Two-center effects in ion-atom Collisions: A Symposium in honor of M. Eugene Rudd, 245–265
- Einstein, A. 1916, *Sitzungsberichte der Koumnlnglich Preussischen Akademie der Wissenschaften*, 688
- Forbush, S. E. 1937, *Physical Review*, 51, 1108
- Forbush, S. E. 1954, *Journal of Geophysical Research*, 59, 525
- Forbush, S. E. 1958, *Journal of Geophysical Research*, 63, 651
- Furman, M. A. & Pivi, M. T. F. 2002, *Phys. Rev. ST Accel. Beams*, 5, 124404
- García Marirrodriga, C., Pacros, A., Strandmoe, S., et al. 2021, *A&A*, 646, A121
- Geant4 Collaboration. 2024, *Geant4 Physics Reference Manual*, accessed: 2024-09-12
- Gleeson, L. J. & Axford, W. I. 1968, *ApJ*, 154, 1011
- Grimani, C. 2004, *A&A*, 418, 649
- Grimani, C. 2007, *A&A*, 474, 339
- Grimani, C., Andretta, V., Antonucci, E., et al. 2023a, *A&A*, 677, A45
- Grimani, C., Andretta, V., Chioetto, P., et al. 2021, *A&A*, 656, A15
- Grimani, C., Cesarini, A., Fabi, M., et al. 2020a, *The Astrophysical Journal*, 904, 64
- Grimani, C., Cesarini, A., Fabi, M., & Villani, M. 2020b, *Classical and Quantum Gravity*, 38, 045013
- Grimani, C., Fabi, M., Finetti, N., Laurenza, M., & Storini, M. 2013, in *Journal of Physics Conference Series*, Vol. 409, *Journal of Physics Conference Series*, 012159
- Grimani, C., Fabi, M., Finetti, N., & Tombolato, D. 2008, *International Cosmic Ray Conference*, 1, 485
- Grimani, C., Fabi, M., Finetti, N., & Tombolato, D. 2009, *Class. Quant. Grav.*, 26, 215004
- Grimani, C., Fabi, M., Lobo, A., Mateos, I., & Telloni, D. 2015, *CQG*, 32, 035001
- Grimani, C., Fabi, M., Sabbatini, F., & Villani, M. 2025, in preparation
- Grimani, C., Fabi, M., Sabbatini, F., et al. 2023b, *Astrophys and Space Science*, 368, 78
- Grimani, C., Villani, M., Fabi, M., Cesarini, A., & Sabbatini, F. 2022, *A&A*, 666, A38
- Grimani, C., Villani, M., Fabi, M., & Sabbatini, F. 2024, *Journal of High Energy Astrophysics*, 42, 38
- Incerti, S., Baldacchino, G., Bernal, M., et al. 2010a, *International Journal of Modeling, Simulation, and Scientific Computing*, 01, 157
- Incerti, S., Ivanchenko, A., Karamitros, M., et al. 2010b, *Medical Physics*, 37, 4692
- Incerti, S., Kyriakou, I., Bernal, M. A., et al. 2018, *Medical Physics*, 45, e722
- Ivanchenko, V., Incerti, S., Allison, J., et al. 2014, in *Geant4 electromagnetic physics: improving simulation performance and accuracy*, 03101
- Mazzanti, D., Guberman, D., Aran, A., et al. 2023, *PoS, ICRC2023*, 1494
- Miroshnichenko, L. I., De Koning, C. A., & Perez-Enriquez, R. 2000, *Space Sci. Rev.*, 91, 615
- Moskalenko, I. V. & Strong, A. W. 1998, *Ap. J.*, 493, 694
- Müller, D., St. Cyr, O. C., Zouganelis, I., et al. 2020, *A&A*, 642, A1
- Muratore, M. 2023, *PRD*, 108, 082004
- Muratore, M., Hartwig, O., Vetrugno, D., Vitale, S., & Weber, W. J. 2023, *Phys. Rev. D*, 107, 082004
- Papini, P., Grimani, C., & Stephens, S. 1996, *Nuovo Cim.*, C19, 367
- Quang Nam, D., Martino, J., Lemièrre, Y., et al. 2023, *Phys. Rev. D*, 108, 082004
- Reames, D. V. 2021, *Solar Energetic Particles. A Modern Primer on Understanding Sources. Acceleration and Propagation*, Vol. 978
- Reames, D. V. 2022, *Frontiers in Astronomy and Space Sciences*, 9
- Rodríguez-Pacheco, J., Wimmer-Schweingruber, R. F., Mason, G. M., et al. 2020, *A&A*, 642, A7
- Sakata, D., Incerti, S., Bordage, M. C., et al. 2016, *Journal of Applied Physics*, 120, 244901
- Sakata, D., Kyriakou, I., Okada, S., et al. 2018, *Medical Physics*, 45, 2230, epub 2018 Mar 23
- Schou, J. 1980, *Phys. Rev. B*, 22, 2141
- Sesana, A. 2016, *Phys. Rev. Lett.*, 116, 231102
- Shaul, D. N. A., Aplin, K. L., Araújo, H., et al. 2006, in *American Institute of Physics Conference Series*, Vol. 873, *Laser Interferometer Space Antenna: 6th International LISA Symposium*, ed. S. M. Merkowitz & J. C. Livas (AIP), 172–178
- Shikaze, Y., Haino, S., Abe, K., et al. 2007, *Astroparticle Physics*, 28, 154
- Simpson, J. A. 1983, *Annual Review of Nuclear and Particle Science*, 33, 323
- Singh, A. K. & Bhargawa, A. 2019, *Ap&SS*, 364, 12
- Suwa, Y. & Murase, K. 2009, *Phys. Rev. D*, 80, 123008
- Taioli, S., Dapor, M., Dimiccoli, F., et al. 2023, *Classical and Quantum Gravity*, 40, 075001
- Tinto, M. & Armstrong, J. W. 1999, *Phys. Rev. D*, 59, 102003
- Tran, H. N., Archer, J., Baldacchino, G., et al. 2024, *Medical Physics*, n/a [<https://aapm.onlinelibrary.wiley.com/doi/pdf/10.1002/mp.17256>]
- Usoskin, I. G., Bazilevskaya, G. A., & Kovaltsov, G. A. 2011, *Journal of Geophysical Research: Space Physics*, 116
- Usoskin, I. G., Gil, A., Kovaltsov, G. A., Mishev, A. L., & Mikhailov, V. V. 2017, *Journal of Geophysical Research: Space Physics*, 122, 3875
- Van Hove, M., Weinberg, W., & Chan, C. 1986, *Low-Energy Electron Diffraction: Experiment, Theory and Surface Structure Determination*, Springer Series in Surface Sciences (Springer Berlin Heidelberg)
- Vidano, S., Novara, C., Pagone, M., & Grzymisch, J. 2022, *Acta Astronautica*, 193, 731

- Villani, M., Benella, S., Fabi, M., & Grimani, C. 2020, *Applied Surface Science*, 512, 145734
- Villani, M., Cesarini, A., Fabi, M., & Grimani, C. 2021, *CQG*, 38, 145005
- Villani, M., Fabi, M., Grimani, C., et al. 2024a, *Results in Physics*, 60, 107638
- Villani, M., Sabbatini, F., Cesarini, A., Fabi, M., & Grimani, C. 2024b, *Experimental Astronomy*, 58, 15
- Villani, M., Sabbatini, F., Grimani, C., Fabi, M., & Cesarini, A. 2023, *Experimental Astronomy*, 56, 1
- Vlachoudis, V. 2009, in *International Conference on Mathematics, Computational Methods & Reactor Physics (M&C 2009)*, Saratoga Springs, New York, 790–800
- Vocca, H., Grimani, C., Amico, P., et al. 2004, *Classical and Quantum Gravity*, 21, S665
- Wass, P. J., Araújo, H. M., Shaul, D. N. A., & Sumner, T. J. 2005, *Classical and Quantum Gravity*, 22, S311
- Wass, P. J., Sumner, T. J., Araújo, H. M., & Hollington, D. 2023, *Phys. Rev. D*, 107, 022010